Title

The mechanistic implications of the high temperature, long time thermal stability of nanoscale Mn-Ni-Si precipitates in irradiated reactor pressure vessel steels

Authors

Almirall, N
Wells, PB
Pal, S
et al.

Publication Date

2020-05-01

DOI

10.1016/j.scriptamat.2020.02.027

Peer reviewed

The Mechanistic Implications of the High Temperature, Long Time Thermal Stability of Nanoscale Mn-Ni-Si Precipitates in Irradiated Reactor Pressure Vessel Steels

N. Almirall[a], P. B. Wells[a,1], Soupitak Pal[a], P. D. Edmondson[b], T. Yamamoto[a], K. Murakami[c], G. R. Odette[a]

[a)] Materials Department, University of California, Santa Barbara, CA 93106
[b)] Materials Science and Technology Division, Oak Ridge National Laboratory, Oak Ridge, TN 37831
[c)] Nuclear Professional School, The University of Tokyo, Tokai, Ibaraki, Japan, 318-119
[1)] Current affiliation: Intel Corporation, Hillsboro, OR 97124

Corresponding Author

G. Robert Odette
Distinguished Research Professor Emeritus,
UCSB Mechanical Engineering and Materials Departments
Email: odette@engineering.ucsb.edu
Phone: (805) 964-5586
Fax: (805) 893-8651

Address:
Mechanical Engineering Department
2355 Engineering II
University of California, Santa Barbara
Santa Barbara, CA 93106-5070

Abstract

Post irradiation annealing (PIA) clarified the induced versus enhanced controversy regarding nanoscale Mn-Ni-Si precipitate (MNSP) formation in pressure vessel steels. Radiation induced MNSPs would dissolve under high temperature PIA, while radiation enhanced precipitates would be stable above a critical radius (r_c). A Cu-free, high Ni steel was irradiated with 2.8MeV Fe^{2+} ions at two temperatures to generate MNSPs with average radii ($\bar{r}$) above and below an estimated r_c for PIA at 425°C up to 52 weeks. Atom probe tomography and energy dispersive x-ray spectroscopy showed MNSPs with $r < r_c$ dissolved, while those with $r > r_c$ slightly coarsened, consistent with thermodynamic predictions.

Key Words: *Radiation damage; Atom probe tomography; Precipitation; Irradiation embrittlement; Reactor pressure vessel steels*

Life extension of light water reactors (LWRs) is important to sustaining nuclear power as the largest contributor to C-free electricity [1]. One of the main life-limiting components of LWRs is the massive reactor pressure vessel (RPV), which becomes increasingly embrittled by exposure to neutrons emanating from the reactor core [2,3]. Accurately predicting RPV embrittlement is required to ensure large safety margins against vessel fracture. Unfortunately, current regulatory models underpredict embrittlement at high, extended-life neutron fluence in accelerated higher flux test reactor experiments. Thus, a major focus of this research is to develop high fluence, low flux embrittlement models.

The underprediction of embrittlement at high fluence is primarily attributed to the delayed formation of large volume fractions (f) of Mn-Ni-Si precipitates (MNSPs), which are not accounted for in current regulatory models [4–8]. The existence of MNSPs has been demonstrated in both surveillance and test reactor irradiations [4,9–22], but their detailed character and formation mechanisms is one of the most highly debated issues in the field of radiation effects [4,14,23–26]. The central question relates to the driving force for MNSP formation. Thermodynamic models predict that: a) MNSPs are nm-scale variants of equilibrium G and Γ_2 phases in typical low alloy Mn (0.8 to 1.6 at.%), Ni (0.2 to 1.6 at.%) and Si (0.3 to 1.2 at.%) bearing RPV steels; and, b) MNSP formation is accelerated at low service temperatures, around 290°C, by the excess defect concentrations under irradiation, and corresponding radiation enhanced diffusion (RED) rates [4,14,26–28]. Others propose that MNSPs are not thermodynamic phases, but rather are formed, grown ***and*** sustained by radiation induced solute segregation (RIS) to defect sinks [23–25,29], such as dislocation loops, vacancy clusters [23,24,30] and network dislocations [25,31]. Clarifying MNSP formation mechanisms is important, not only for developing advanced models to predict embrittlement over extended RPV operation, but also for guiding development of new irradiation tolerant alloys.

Post irradiation annealing (PIA) can provide significant insight into the nature of MNSPs. For example, solute clusters that form by a RIS mechanism would dissolve during PIA, while enhanced thermodynamic phases should be stable, or even grow and ultimately coarsen. However, two issues complicate this simple picture:

1. Thermal dissolution, or growth and coarsening, kinetics are very slow at the low irradiation temperatures around 290°C. Thus PIA studies must be conducted for long times (t_a), at much higher temperatures (T_a), which obviously affects the thermodynamics.
2. The Gibbs-Thomson effect is very important at small nm-scale precipitate sizes. Precipitates below a critical radius (r_c) at high PIA temperature will dissolve in a solute depleted matrix, even if they are a thermally stable bulk phase.

In a recent ,425°C PIA study up to 57 weeks, of a nearly fully phase separated highly 320°C neutron

irradiated, Cu free, 1.6 at.% Ni RPV steel, atom probe tomography (APT) showed that most MNSPs dissolved, although a very low density of larger MNSPs with r > 2.2 nm, remained and appeared to coarsen at long times [16]. While, the APT MNSP statistics were limited, scanning transmission electron microscopy-energy dispersive X-ray spectroscopy (STEM-EDS) characterization confirmed the stability of the larger MNSPs. These results are consistent with cluster dynamics and kinetic lattice Monte Carlo models [16,32], which predict a large reduction in precipitate number density (N) at small $r < r_c$ at the high PIA temperature of 425°C, in a solute depleted matrix. Thus to further explore the thermal stability of MNSPs, we designed and carried out a special heavy ion irradiation experiment for the same Cu free high Ni steel.

Ion irradiations can produce precipitates in RPV steels that are essentially the same as those formed under neutron irradiation, albeit they require a higher damage doses expressed in terms of displacements per atom (dpa) [33–35]. However, ion irradiations are much more flexible, inexpensive, rapid and are absent any specimen radioactivity. Here, we used two separate 2.8MeV self Fe^{2+}-ion irradiation sequences to create populations of precipitates that targeted average radii ($\bar{r}$) that were both above and below the estimated r_c, again in the Cu-free 1.6 wt.% Ni steel cited above. One low-high (LH) ion irradiation was split into two temperature increments of 2.5 dpa each: 2.5 dpa at 330°C to nucleate a high N of MNSPs, followed by an increment at 2.5 dpa at 400°C to grow them to a volume fraction f, close to full phase separation, but with $\bar{r} < r_c$. A second high temperature (HH) irradiation to 2.5 dpa at 400°C was aimed at producing a lower N of MNSPs with approximately the same f and larger $\bar{r} > r_c$. For thermally stable MNSPs, those larger than r_c should remain and even grow and ultimately coarsen; while those that are smaller than r_c should fully dissolve. The growth of the larger MNSPs is due to re-precipitation of solutes that initially dissolved during PIA. Note the actual r_c varies with t_a, since the dissolved solute concentrations change with dissolution and re-precipitation [16].

APT maps demonstrate that the LH and HH irradiations were successful in generating a wide range of MNSP sizes, with $\bar{r}$ of 1.74 nm (LH) and 2.67 (HH), respectively. These as-irradiated (AI) alloys were then annealed at 425°C for up to 52 weeks. The main goal was to distinguish between RIS or RED formation mechanisms, associated with the MNSP thermal stability, or lack thereof, in comparison to thermodynamic predictions of r_c.

Note, even if it is shown that the MNSPs are stable, and the driving force for forming MNSPs is largely thermodynamic, RIS may affect the precipitate compositions somewhat [11]. Indeed, it is important to emphasize that RIS and RED work in tandem, and both can and do play a role in MNSP evolution in RPV and other steels. Most notably, MNSPs in low Cu steels are often associated with solute segregation to dislocations (loops and network); for example, see [4]. These associations are partly due to RIS, but are

also partly thermodynamic in origin [25]. That is, both RIS and dislocation-modified thermodynamics result in locally enriched microalloy compositions, where MNSP formation rates are much higher than in the matrix. This can be described as dislocations resulting in significant alterations of the local thermodynamics and effective phase boundaries [25]. However, this topic is beyond the scope of this short paper[1]. Additional general background on embrittlement can be found in, for example [4,36,37].

The nominal composition of the essentially Cu-free high Ni split-melt bainitic RPV steel studied here, designated as CM6, is 0.02 Cu, 1.57 Ni, 1.5 Mn, 0.31 Mo, 0.012 P, 0.68 C, 0.33 Si, bal. Fe in units of at.%. The standard heat treatment is given in the supplemental information (SI). The resulting small heat, split-melt alloy microstructure and properties are fully representative of actual RPV steels. Small 1.5x0.5 mm disc specimens were irradiated with 2.8 MeV Fe^{2+} ions in the High Fluence Irradiation Facility (HIT), at the University of Tokyo facility in Japan at ≈ 330°C and 400°C (LH) and 400°C (HH) conditions. The average dpa rate was ≈ $1.5x10^{-4}$ dpa/s, yielding a dose of 5.0 and 2.5 dpa, respectively, at a depth of 500 nm. SRIM 2008 was used to calculate the dpa as a function of depth as shown in the SI Figure S1. The dpa were based on the Kinchin-Pease model, with a displacement energy of 40 eV, as recommended in ASTM E521-96 (2009) [38,39]. Other information on the irradiation is included in the SI. The PIA treatments were in vacuum at 425°C for 22 and 52 weeks.

The previous PIA study of neutron irradiated CM6 showed that MNSPs below r_c ≈ 2.2 nm re-dissolved in much shorter times at 425°C, assuring that the 52 week PIA results will not be affected by kinetics [16]. Standard FIB liftouts (see SI) were extracted and fabricated into APT tips and TEM foils at a depth of ≈ 400-600 nm from the surface, where the damage profile is relatively flat. APT and STEM-EDS was used to characterize the MNSPs. Details of the standard STEM-EDS methods are given in the SI. The APT method is more generally described elsewhere [40–42]. Note, the matrix Fe atoms nominally in the precipitates is likely an artifact, and are not included in the MNSPs [20,43–46].

While the APT technique offers very high spatial resolution and detailed measurements of precipitate N(r), f and composition, only a very small sampling volume is probed. This is an issue at longer t_a, when precipitate populations may be low and vary from tip to tip, due to differences in the local compositions. Thus to complement the APT, STEM-EDS was performed using the FEI TALOS F200X S/TEM in the Low Activation Materials Development and Analysis Laboratory at ORNL, to characterize N(r), and $\bar{r}$ in much larger volumes. Clearly the two techniques are highly complementary and, as shown below, paint a

[1] Thermal solute segregation to dislocations, in some cases leading to the formation of precipitates, have been recently described in a growing "linear complexions" literature, which we will not attempt to cite here. Along with RIS, thermal segregation is under investigation in our work. However, while it is an exciting direction of research, this topic is beyond the scope of this short Scripta Materialia paper, which focuses on the thermal stability of MNSPs.

clear and self-consistent picture of the thermal stability of the MNSPs as a function of their AI N(r) and $\bar{r}$. Tables 1 and 2 summarize the APT and STEM-EDS data, respectively.

Table 1. An APT precipitate summary for the high low Cu, high Ni steel (CM6) for the AI and 425°C annealed conditions.

		Average t_a, $\bar{r}$, N and f[a]			Average Matrix Composition (at.%)			Average Precipitate Composition (at.%)			Artifact Fe[b]	10^6 atoms
	t_a	$\bar{r}$	N	f	Ni	Mn	Si	Ni	Mn	Si		
330/400	0	1.74±0.17	9.50±0.53	1.97±0.23	0.28	0.74	0.04	57.8	28.4	13.8	57.0	40.8
330/400	22	2.40	0.40	0.20	1.31	1.25	0.30	51.0	33.4	15.6	47.6	13.0
330/400	52	N/A	N/A	N/A				-	-	-		-
400	0	2.61±0.03	3.00±1.06	1.88±0.62	0.65	1.48	0.06	64.0	15.9	20.1	47.1	23.4
400	22	2.30	1.95	0.88	1.16	1.39	0.30	53.4	33.2	13.4	49.4	7.5
400	52	2.82±0.05	1.76±0.17	1.65±0.09	0.68	0.99	0.08	54.0	31.0	15.0	35.9	4.4

*a) Units: t_a (wks), $\bar{r}$ (nm), N (10^{23} m^{-3}), f (%). b) The nominal IVAS Fe found in all the MNSPs, that is thought to largely be an artifact.

Table 2: An EDS precipitate summary for the low Cu, high, high Ni steel (CM6) for the AI and 425°C annealed conditions.

		Average EDS t_a, $\bar{r}$ *and* N[a]	
	t_a	$\bar{r}$	N
330/400	0	4.40±0.80	3.22±.50
330/400	22	4.34±2.20	0.37±0.20
330/400	52	7.12±0.22	0.02±0.01
400	0	6.62±0.82	0.78±0.28
400	52	7.86±1.21	0.51±0.14

*a) Units: t_a (wks), $\bar{r}$ (nm), N (10^{23} m^{-3}).

Figure 1 summarizes the results of the APT measurements. Figures 1a and d show the MNSP N(r) for the various conditions. Figures 1b and e show corresponding examples of the APT reconstructions. Figures 1c and f plot N, $\bar{r}$ and f as a function of t_a. Figure 2 similarly summarizes the STEM-EDS data. In this case, the Ni MNSPs, which also contain Mn and Si, are shown in Figures 2b and e. The APT and STEM-EDS results are qualitatively similar. The major difference is that the EDS measurements do not observe smaller MNSPs, while they better quantify the N at larger r. Figure 2g shows the MNSP composition in the various conditions are similar, except in the case of the HH AI condition, which has higher and lower than average Ni and Mn contents, respectively.

These results show that essentially all of the smaller MNSPs, in the LH AI condition, dissolve by 22 weeks. Note that, in this case, the somewhat lower Ni content in in the LH APT tips also enhanced dissolution. More significantly, however, the initially larger MNSPs in the HH AI condition undergo relatively little change for PIA at 425°C for t_a up to 52 weeks. More specifically, Figure 1f shows that the HH N systematically decreases up to 52 weeks, while $\bar{r}$ first decreases slightly, and then increases, indicating a small amount of MNSP regrowth and coarsening. The corresponding f also first decreases and then increases to values similar to that in the AI condition. The complementary HH STEM-EDS data in Figure 2 also show slight MNSP coarsening at 52 weeks. Note, not surprisingly, the r values measured by STEM-EDS are systematically larger and N lower than observed in the APT studies. The $\bar{r}$, N and f trends are expected and are well-predicted by a cluster dynamics and KLMC annealing models [16,32]. In the initially AI solute depleted matrix, the critical radius (r_c) is very large at 425°C. But as the MNSPs dissolve, and solutes reenter the matrix, r_c decreases. MNSPs with r that are greater than r_c then grow. A simple analysis of r_c is discussed next.

The MNSP compositions are generally consistent with the Γ_2 phase, with the exception of the AI HH condition, which is compositionally closer to the G phase. Note, the HH tips contained an larger Ni and lower Mn than average, respectively. The Γ_2 phase is formed by the reaction: 3Ni(s) + 2Mn(s) + 1Si(s)$\Leftrightarrow$$Ni_3Mn_2Si$ (nominal), where subscript s denotes dissolved solutes. At equilibrium, $\{[X_{Ni}]^3[X_{Mn}]^2[X_{Si}]\}^{1/6} = K(T)$, where X_i are the dissolved solutes mole fractions and K(T) is the temperature dependent reaction constant, incorporating the activity coefficients of the dissolved solutes and the formation free energy of the Γ_2 phase. Ke used CALPHAD to determine K(T), which is ≈ 0.008 at 425°C [22]. The solute supersaturation is $S = [X_{ni}]^3[X_{mn}]^2[X_{si}]\}^{1/6}/K(425°C)$ and the corresponding free precipitation energy change is $\Delta G_v=-[RT/V_m]\ln[S]$, where R is the gas constant and V_m is the Fe molar volume. The critical radius is $r_c=-2\gamma_{pm}/\Delta G_v$, where the interface energy is γ_{pm} = 0.175 J/m^2. The corresponding HH r_c for the matrix compositions in Table 2 are 2.07 nm (22 weeks) and 2.53 nm (52 weeks). For the G phase, nominally $Ni_{16}Mn_6Si_7$, r_c=2.5nm (22 weeks) and 3.49 nm (52 weeks).

These r_c estimates are very consistent with the observed HH MNSP stability. Figure 3a shows the calculated Ni phase boundary solvus line (X_{Nis}) as a function of temperature for stoichiometric G and Γ_2 phases [47]. Notably the X_{Nis} is ≈ 3.5 times lower at 290°C versus 425°C. The filled circles are the measured matrix X_{Nim} in the AI (400°C) and HH 52-week PIA (425°C) conditions, which are consistent with the computed X_{Nis}. However, the Gibbs Thomson effect, $X_{Nis} = X_{Nim}\exp(-2\gamma_{pm}V_m/rRT)$, would suggest that the actual equilibrium X_{Nis} is lower, as shown as the blue squares. The adjusted X_{Nis} agreement with the predicted solvus is not as good, but it is still reasonable. Figure 3b shows a semitransparent EDS map of

the MNSPs (Ni-red) overlaying a dark field TEM micrograph of the dislocation structure in the LH 52 week condition. The arrows show that most of the MNSPs are associated with dislocations, consistent with previous observations of 425°C PIA after a high dpa neutron irradiation [16].

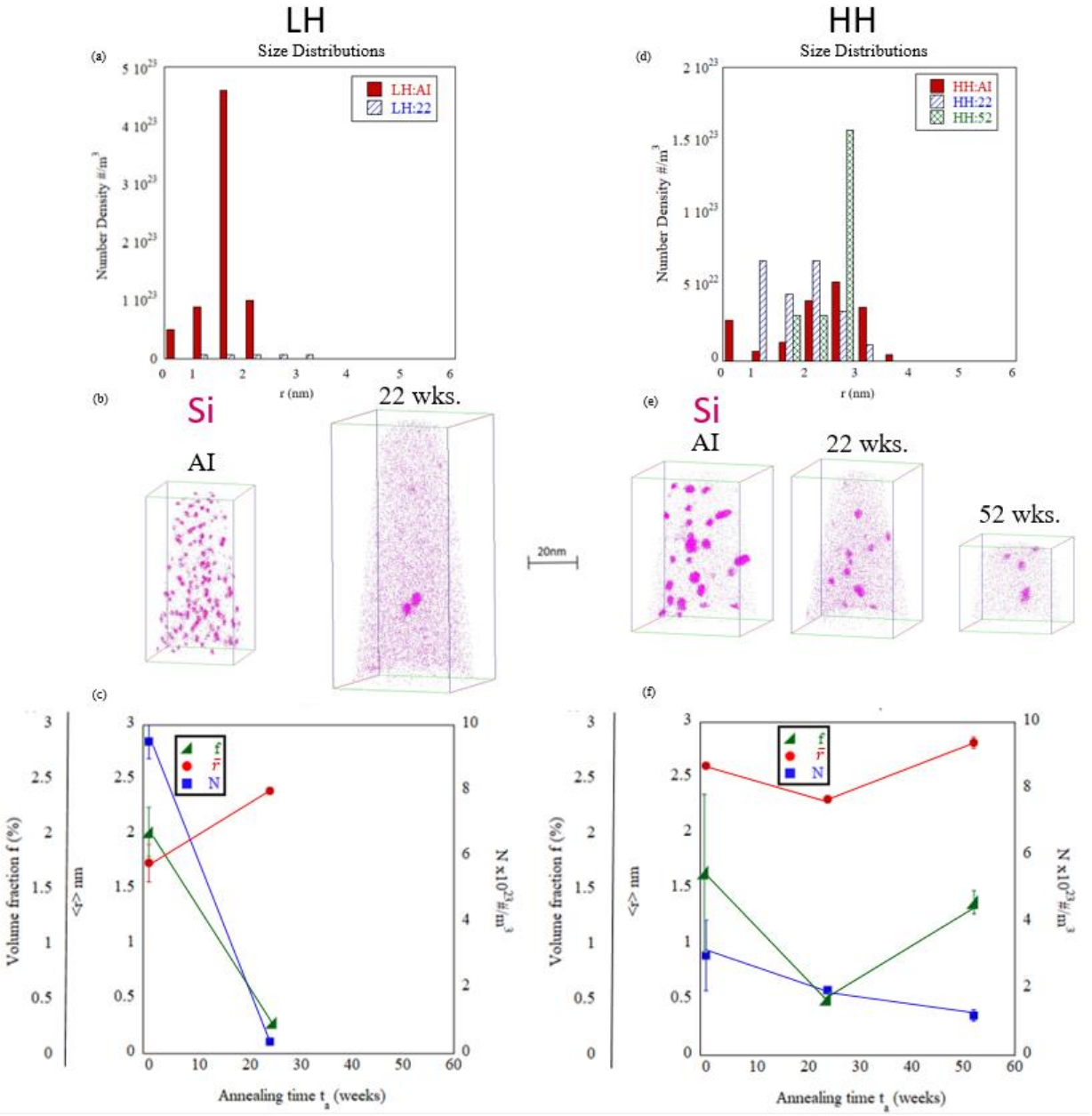

Figure 1. a) and d) APT N(r) for the LH and HH conditions, respectively; b) and e) examples of APT reconstruction for the LH and HH conditions, respectively; and, c) and f) N, $\bar{r}$ and f for the LH and HH conditions, respectively.

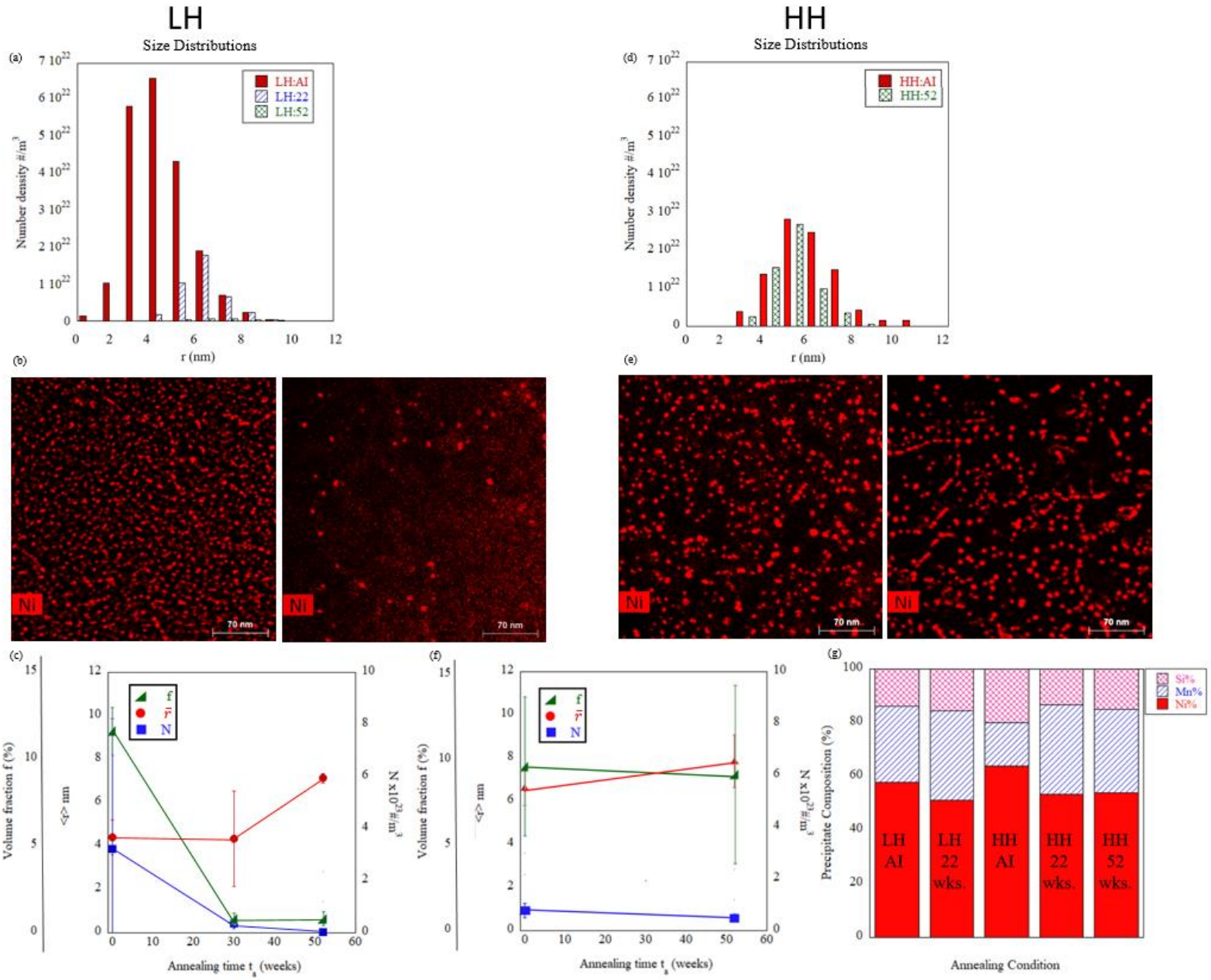

Figure 2. a) and d) STEM-EDS N(r) for the LH and HH conditions, respectively; b) and e) STEM-EDS micrographs of Ni in the Mn-Ni-Si precipitates for the LH and HH conditions, respectively; and, c) and f) and f) N, $\bar{r}$ and f for the LH and HH conditions, respectively; and g) bar graphs comparing the Ni, Mn, and Si precipitate compositions for various conditions.

In summary, ion irradiations and long term annealing at 425°C successfully probed the thermal stability of MNSPs larger (irradiated at 400°C) and smaller (irradiated at 330°C and 400°C) than r_c. Analysis of the data generated by these complementary techniques leads to the following conclusions:

- MNSPs that are both larger and smaller than r_c were generated in high Ni (~1.6 at.%) RPV steel CM6 by varying the ion irradiation temperature sequence.
- The smaller precipitates in LH condition, with $r < r_c$, largely dissolve after annealing at 425°C for long times.
- The larger precipitates in the HH condition, with $r > r_c$, are stable.
- Thus it must be concluded that the MNSPs are thermodynamically stable, and are likely the Γ_2 phase in most cases.
- The MNSPs would be even more thermodynamically stable at much lower neutron irradiation RPV service temperatures around 290°C
- The MNSPs in the HH 52 week condition are largely associated with network dislocations.

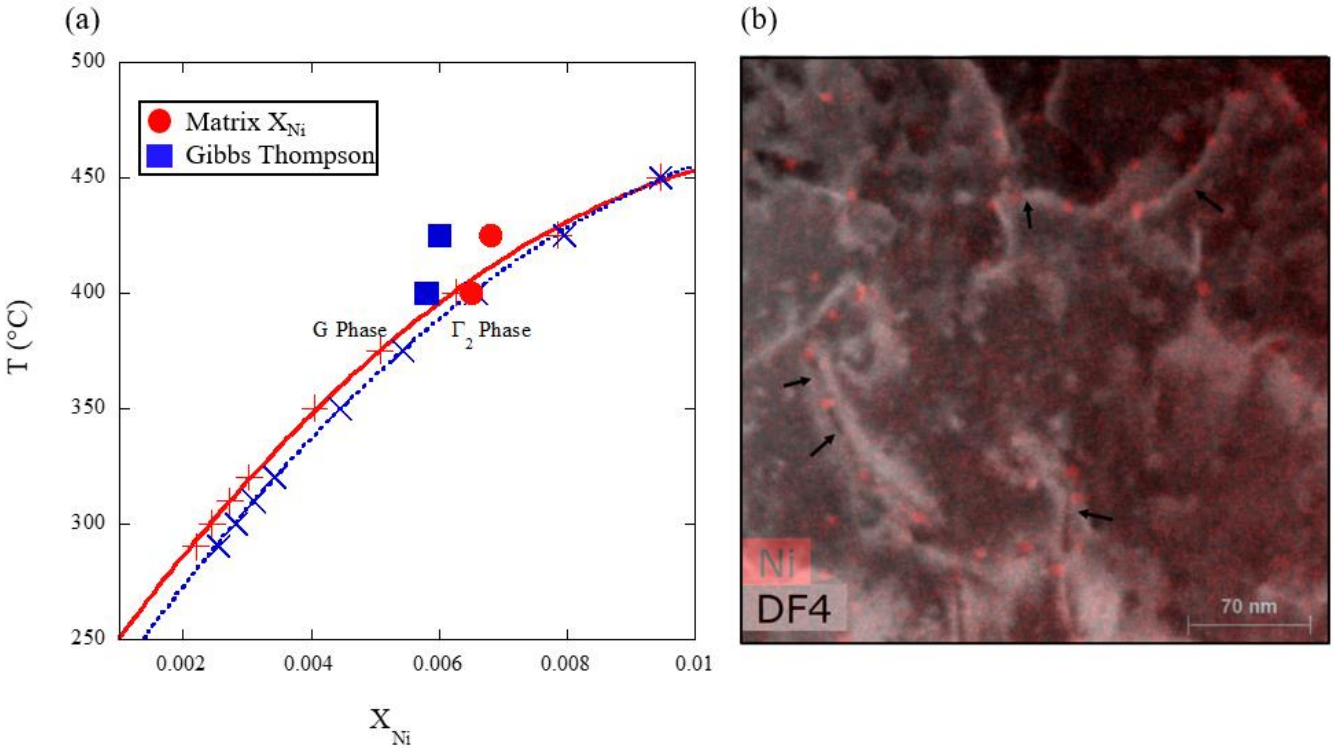

Figure 3. a) Calculated Ni Phase boundary solvus lines (X_{Nis}) as a function of temperature for G and Γ_2 phases along with the measured matrix Ni compositions, X_{Nim} (filled red circles), in the HH AI and 52 week PIA conditions, as well as the Gibbs Thompson adjusted X_{Nis} (blue filled squares) based on the matrix X_{Nim}; and, b) dark field micrograph of the dislocations overlaid with a partially transparent image of the Ni EDS signal (red spots) for the associated MNSPs LH 52 week PIA condition.

REFERENCES

[1] Climate Change and Nuclear Power 2018, International Atomic Energy Agency. Vienna (2018).

[2] J.T. Busby, Light Water Reactor Sustainability Materials Aging and Degrdation Pathway Technical Program Plan ORNL/LTR-2012/327, (2012).

[3] Expanded Materials Degrdation Assessment (EDMA): Aging of Reactor Pressure Vessels NUREG/CR-7153 V3, (2013).

[4] G.R. Odette, T. Yamamoto, T.J. Williams, R.K. Nanstad, C.A. English, On the history and status of reactor pressure vessel steel ductile to brittle transition temperature shift prediction models, J. Nucl. Mater. 526 (2019) 151863. doi:10.1016/j.jnucmat.2019.151863.

[5] E.D. Eason, G.R. Odette, R.K. Nanstad, T. Yamamoto, A physically-based correlation of irradiation-induced transition temperature shifts for RPV steels, J. Nucl. Mater. 433 (2013) 240–254. doi:10.1016/j.jnucmat.2012.09.012.

[6] ASTM Subcommittee E10.02, Adjunct for ASTM E900-15: Technical Basis for the Equation used to Predict Radiation-Induced Transition Temperature shift in Reactor Vessel Materials, ASTM International, West Conshohocken, PA, 2015.

[7] P.N. Randall, Basis for Revision 2 of the US Regulatory Commission's Regulatory Guide 1.99, Radiation Embrittlement of Nuclear Reactor Pressure Vessels an International Review (Second Volume), ASTM STP 909-2, ASTM (1986) pp. 149–162.

[8] U.S. Nuclear Regulatory Commission, Radiation Embrittlement of Reactor Vessel Materials, Regulatory Guide 1.99 Rev. 2, 1988.

[9] G.R. Odette, T. Yamamoto, B.D. Wirth, Late Blooming phases and Dose Rate Effects in RPV Steels: Integrated Experiments and Models, Proceeding of the Second International Conference on Multiscale Modeling, October 11-15, 2004, Los Angeles, CA (2004) pp. 10.

[10] D.J. Sprouster, J. Sinsheimer, E. Dooryhee, S.K. Ghose, P. Wells, T. Stan, N. Almirall, G.R. Odette, L.E. Ecker, Structural characterization of nanoscale intermetallic precipitates in highly neutron irradiated reactor pressure vessel steels, Scr. Mater. 113 (2016) 18–22. doi:10.1016/j.scriptamat.2015.10.019.

[11] N. Almirall, P.B. Wells, T. Yamamoto, K. Wilford, T. Williams, N. Riddle, G.R. Odette, Precipitation and Hardening in Irradiated Low Alloy Steels with a Wide Range of Ni and Mn Compositions, Acta Mater. 179 (2019) 119–128. doi:10.1016/j.actamat.2019.08.027.

[12] M.G. Burke, R.J. Stofanak, J.M. Hyde, C.A. English, W.L. Server, Microstructural aspects of irradiation damage in A508 Gr 4N forging steel: Composition and flux effects, J. ASTM Int. 1 (2002) 1–14. doi:10.1520/jai11773.

[13] M.K. Miller, K.A. Powers, R.K. Nanstad, P. Efsing, Atom probe tomography characterizations of high nickel, low copper surveillance RPV welds irradiated to high fluences, J. Nucl. Mater. 437 (2013) 107–115. doi:10.1016/j.jnucmat.2013.01.312.

[14] H. Ke, P. Wells, P.D. Edmondson, N. Almirall, L. Barnard, G.R. Odette, D. Morgan, Thermodynamic and kinetic modeling of Mn-Ni-Si precipitates in low-Cu reactor pressure vessel steels, Acta Mater. 138 (2017) 10–26. doi:10.1016/j.actamat.2017.07.021.

[15] M.K. Miller, M.A. Sokolov, R.K. Nanstad, K.F. Russell, APT characterization of high nickel RPV steels, J. Nucl. Mater. 351 (2006) 187–196. doi:10.1016/j.jnucmat.2006.02.013.

[16] N. Almirall, P.B. Wells, H. Ke, P. Edmondson, D. Morgan, T. Yamamoto, G.R. Odette, On the elevated temperature thermal stability of nanoscale Mn-Ni-Si precipitates formed at lower temperature in highly irradiated reactor pressure vessel steels, Sci. Rep. 9 (2019). doi:10.1038/s41598-019-45944-z.

[17] M.K. Miller, K.F. Russell, Embrittlement of RPV steels: An atom probe tomography perspective, J. Nucl. Mater. 371 (2007) 145–160. doi:10.1016/j.jnucmat.2007.05.003.

[18] T. Takeuchi, A. Kuramoto, J. Kameda, T. Toyama, Y. Nagai, M. Hasegawa, T. Ohkubo, T. Yoshiie, Y. Nishiyama, K. Onizawa, Effects of chemical composition and dose on microstructure evolution and hardening of neutron-irradiated reactor pressure vessel steels, J. Nucl. Mater. 402 (2010) 93–101. doi:10.1016/j.jnucmat.2010.04.008.

[19] P.B. Wells, T. Yamamoto, B. Miller, T. Milot, J. Cole, Y. Wu, G.R. Odette, Evolution of manganese–nickel–silicon-dominated phases in highly irradiated reactor pressure vessel steels, Acta Mater. 80 (2014) 205–219. doi:10.1016/j.actamat.2014.07.040.

[20] P.B. Wells, The Character and Stability of Mn-Ni-Si Precipitates in Reactor Pressure Vessel Steels [PhD Thesis], Univ. Calif. St. Barbar. (2015).

[21] P.D. Styman, J.M. Hyde, D. Parfitt, K. Wilford, M.G. Burke, C. A. English, P. Efsing, Post-irradiation annealing of Ni–Mn–Si-enriched clusters in a neutron-irradiated RPV steel weld using Atom Probe Tomography, J. Nucl. Mater. 459 (2015) 127–134. doi:10.1016/j.jnucmat.2015.01.027.

[22] P.D. Edmondson, M.K. Miller, K.A. Powers, R.K. Nanstad, Atom probe tomography characterization of neutron irradiated surveillance samples from the R . E . Ginna reactor pressure vessel, J. Nucl. Mater. 470 (2016) 147–154. doi:10.1016/j.jnucmat.2015.12.038.

[23] M. Chiapetto, L. Messina, C.S. Becquart, P. Olsson, L. Malerba, Nanostructure evolution of neutron-irradiated reactor pressure vessel steels: Revised Object kinetic Monte Carlo model, Nucl. Instruments Methods Phys. Res. Sect. B Beam Interact. with Mater. Atoms. 393 (2017) 105–109. doi:10.1016/j.nimb.2016.09.025.

[24] M.J. Konstantinović, I. Uytdenhouwen, G. Bonny, N. Castin, L. Malerba, P. Efsing, Radiation induced solute clustering in high-Ni reactor pressure vessel steel, Acta Mater. 179 (2019) 183–189. doi:10.1016/j.actamat.2019.08.028.

[25] M. I. Pascuet, G. Monnet, G. Bonny, E. Martinez, J. J. H. Lim, M.G. Burke, L. Malerba, Solute precipitation on a screw dislocation and its effects on dislocation mobility in bcc Fe, J. Nucl. Mater. 519 (2019) 265-273. doi:10.1016/j.jnucmat.2019.04.007.

[26] M. Mamivand, P. Wells, H. Ke, S. Shu, G. R. Odette, D. Morgan, CuMnNiSi precipitate evolution in irradiated reactor pressure vessel steels: integrated cluster dynamics and experiments, Acta Mater. 180 (2019) 199-217. doi:10.1016/j.actamat.2019.09.016.

[27] C.L. Liu, G.R. Odette, B.D. Wirth, G.E. Lucas, A lattice Monte Carlo simulation of nanophase compositions and structures in irradiated pressure vessel Fe-Cu-Ni-Mn-Si steels, Mater. Sci. Eng. A. 238 (1997) 202–209. doi:10.1016/s0921-5093(97)00450-4.

[28] S. Shu, P.B. Wells, N. Almirall, G.R. Odette, D.D. Morgan, Thermodynamics and kinetics of core-shell versus appendage co-precipitation morphologies: An example in the Fe-Cu-Mn-Ni-Si system, Acta Mater. 157 (2018) 298–306. doi:10.1016/j.actamat.2018.07.037.

[29] D. Terentyev, X. He, G. Bonny, A. Bakaev, E. Zhurkin, L. Malerba, Hardening due to dislocation loop damage in RPV model alloys: Role of Mn segregation, J. Nucl. Mater. (2015). doi:10.1016/j.jnucmat.2014.11.023.

[30] G. Bonny, D. Terentyev, E.E. Zhurkin, L. Malerba, Monte Carlo study of decorated dislocation loops in FeNiMnCu model alloys, J. Nucl. Mater. 452 (2014) 486–492. doi:10.1016/j.jnucmat.2014.05.051.

[31] J.H. Ke, H. Ke, G.R. Odette, D. Morgan, Cluster dynamics modeling of Mn-Ni-Si precipitates in ferritic-martensitic steel under irradiation, J. Nucl. Mater. 498 (2018) 83–88. doi:10.1016/j.jnucmat.2017.10.008.

[32] S. Shu, P.B. Wells, G.R. Odette, D. Morgan, A kinetic lattice Monte Carlo study of post-irradiation annealing of model reactor pressure vessel steels, J. Nucl. Mater. 524 (2019) 312–322. doi:10.1016/J.JNUCMAT.2019.07.018.

[33] G.S. Was, Fundamentals of Radiation Materials Science, Springer, 2007.

[34] G. Was, Challenges to the use of ion irradiation for emulating reactor irradiation, J. Mater. Res. 30 (2015) 1158–1182. doi:10.1557/jmr.2015.73.

[35] B. Heidrich, S.M. Pimblott, G.S. Was, S. Zinkle, Roadmap for the application of ion beam technologies to the challenges of nuclear energy technologies, Nucl. Instruments Methods Phys. Res. Sect. B Beam Interact. with Mater. Atoms. 441 (2019) 41–45. doi:10.1016/j.nimb.2018.12.022.

[36] G.R. Odette, G.E. Lucas, Recent progress in understanding reactor pressure vessel steel embrittlement, Radiat. Eff. Defects Solids. 144 (1998) 189–231. doi:10.1080/10420159808229676.

[37] G.R. Odette, B.D. Wirth, D.J. Bacon, N.M. Ghoniem, Multiscale-Multiphysics Modeling of Materials : Embrittlement of Pressure-Vessel Steels, MRS Bull. 26 (2001) 176–181. doi:10.1557/mrs2001.39.

[38] R.E. Stoller, M.B. Toloczko, G.S. Was, A.G. Certain, S. Dwaraknath, F.A. Garner, On the use of SRIM for computing radiation damage exposure, Nucl. Instruments Methods Phys. Res. Sect. B Beam Interact. with Mater. Atoms. 310 (2013) 75–80. doi:10.1016/j.nimb.2013.05.008.

[39] ASTM E521, Standard Practice for Neutron Radiation Damage Simulation by Charged Particle Irradiation, Annual Book of ASTM Standards, Vol. 12.02, ASTM International, West Conshohocken, PA.

[40] M.K. Miller, Atom Probe Tomography, Kluwer Academic/Plenum Publishers, 2000.

[41] S.P. Gault, B., Moody, M.P., Cairney, J.M., Ringer, Atom Probe Microscopy, 2012.

[42] E.A. Marquis, J.M. Hyde, Applications of atom-probe tomography to the characterisation of solute behaviours, Mater. Sci. Eng. R Reports. 69 (2010) 37–62. doi:10.1016/j.mser.2010.05.001.

[43] P.D. Edmondson, C.M. Parish, R.K. Nanstad, Using complimentary microscopy methods to examine Ni-Mn-Si-precipitates in highly-irradiated reactor pressure vessel steels, Acta Mater. 134 (2017) 31–39. doi:10.1016/j.actamat.2017.05.043.

[44] S. Shu, B.D. Wirth, P.B. Wells, D.D. Morgan, G.R. Odette, Multi-technique characterization of the precipitates in thermally aged and neutron irradiated Fe-Cu and Fe-Cu-Mn model alloys: Atom probe tomography reconstruction implications, Acta Mater. 146 (2017) 237–252. doi:10.1016/j.actamat.2017.12.006.

[45] N.J. Cunningham, Study of the Structure, Composition, and Stability of Y-Ti-O nm-Scale Features in Nano-Structured Ferritic Alloys [PhD Thesis], Univ. Calif. St. Barbar. (2012).

[46] E.A. Marquis, F. Vurpillot, Chromatic aberrations in the field evaporation behavior of small precipitates, Microsc. Microanal. 14 (2008) 561–570. doi:10.1017/S1431927608080793.

[47] N. Almirall, P.B. Wells, T. Yamamoto, A. Kimura, G.R. Odette, On the Use of Charged Particles to Characterize Precipitation in Irradiated Reactor Pressure Vessel Steels with a Wide Range of Compositions, J. Nucl. Mater. (2020) submitted.

ACKNOWLEDGEMENTS

The authors gratefully acknowledge the Nuclear Science User Facilities (NSUF) program, which funded STEM-EDS at Oak Ridge National Laboratory (ORNL), and DOE Nuclear University Program Fellowship support for the lead author. The Light Water Reactor Sustainability Program (LWRSP) program provided critical support through a subcontract from Oak Ridge National Laboratory (ORNL). The CPI was carried out at the High Fluence Irradiation Facility (HIT) at University of Tokyo in Japan. All the APT studies were conducted at the UCSB California Nano Science Institute (CNSI), which is supported by the National Science Foundation. The STEM-EDS studies were conducted at CNSI and ORNL LAMDA facility using instrumentation provided by the Department of Energy, Office of Nuclear Energy, Fuel Cycle R&D Program and the NSUF program. We are also grateful for our modeling collaboration with Professor Dane Morgan's group at the University of Wisconsin, and especially the work of Drs. Huibin Ke and Mahmood Mamivand. In particular, we note the helpful advice Dr. Ke provided regarding the calculations of critical radii. Finally, we thank our UCSB colleague David Gragg for his many contributions to our work.

Supplemental Information

Materials and Irradiations

The steel heat treatment was: temper at 660°C for 4 h, air cool, then stress relieved at 607°C for 24 h followed by a slow cool at 8°C/h to 300°C, then air cool to room temperature. The resulting disc specimens were irradiated in HIT, at the University of Tokyo facility in Japan, by a rastered ion beam. Temperature control was provided by infrared heating of the back of specimen stage, and a thermal imaging camera monitoring specimen surface temperature, which was first calibrat

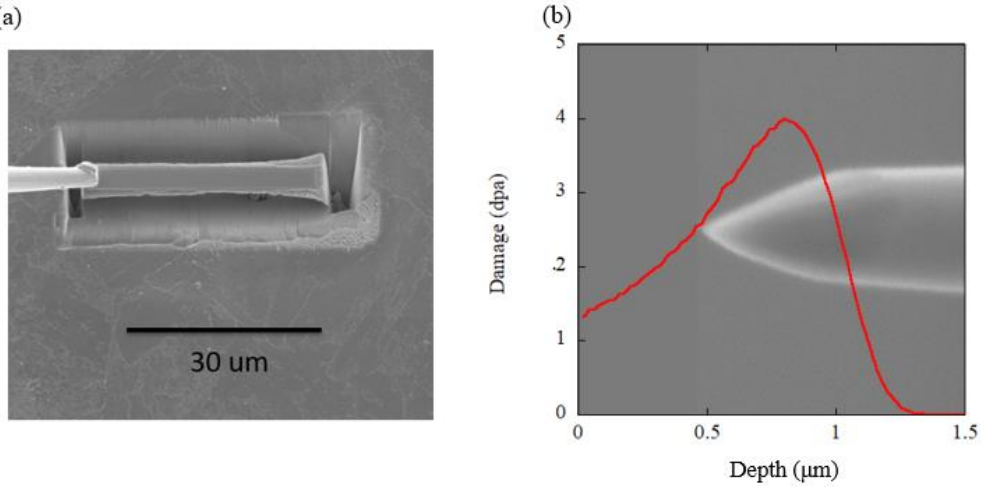

Figure S1. a) A scanning electron microscope image showing the FIB liftout from a charged particle irradiated steel that is subsequently sectioned and mounted onto the micro-tip posts; and, b) annular milling produces a FIB sharpened APT specimen with the SRIM calculated damage as a function of depth overlaid.

Atom Probe Tomography (APT) and Energy Dispersive Spectroscopy (EDS)

APT was performed in voltage mode with a tip temperature of 50K, a pulse fraction of 20%, a target evaporation rate of 0.50%/pulse, and a pulse repetition rate of 200 kHz. IVAS software was used to characterize the clusters, with order K = 5, d_{max} = 0.5-0.6 nm, N_{min} = 20-30 and maximum separation envelope of additional elements (L) = erosion distance of matrix elements (d_{er}) <= d_{max}.The number of solute atoms, corrected for 37% detection efficiency, determined the spherical volume of a MNSP, assuming they have the same atomic volume as Fe. The precipitate r was then taken as the radius of the spherical cluster. The precipitate number

density (N) was calculated by dividing total identified clusters by the total APT tip volume. Clusters that intersect the tip surface were counted as half of a precipitate. The volume fraction of precipitates (f) was determined by dividing the number of solute atoms in all clusters by total number of atoms of a dataset. The STEM-EDS provided high-resolution chemical maps over much larger volume than can be sampled with APT. EDS mapping was performed using a probe size of ~1 nm and current of 1.0 nA, respectively. Analysis of the data was performed using the Bruker-Esprit software.